A New Extensible Continuum Manipulator Using Flexible Parallel Mechanism and Rigid Motion Transmission

Yujiong Liu
Robotics and Mechatronics Lab,
Department of Mechanical Engineering,
Virginia Tech,
Blacksburg, VA 24061
e-mail: yjliu@vt.edu

Pinhas Ben-Tzvi[1]
Robotics and Mechatronics Lab,
Department of Mechanical Engineering,
Virginia Tech,
Blacksburg, VA 24061
e-mail: bentzvi@vt.edu

An extensible continuum manipulator (ECM) has specific advantages over its nonextensible counterparts. For instance, in certain applications, such as minimally invasive surgery or pipe inspection, the base motion might be limited or disallowed. The additional extensibility provides the robot with more dexterous manipulation and a larger workspace. Existing continuum robot designs achieve extensibility mainly through artificial muscle/pneumatic, extensible backbone, concentric tube, and base extension, etc. This article proposes a new way to achieve this additional motion degree-of-freedom by taking advantage of the rigid coupling hybrid mechanism concept and a flexible parallel mechanism. More specifically, a rack and pinion set is used to transmit the motion of the i-th subsegment to drive the (i+1)-th subsegment. A six-chain flexible parallel mechanism is used to generate the desired spatial bending and one extension mobility for each subsegment. This way, the new manipulator can achieve tail-like spatial bending and worm-like extension at the same time. Simplified kinematic analyses are conducted to estimate the workspace and the motion nonuniformity. A proof-of-concept prototype was integrated to verify the mechanism's mobility and to evaluate the kinematic model accuracy. The results show that the proposed mechanism achieved the desired mobilities with a maximum extension ratio of 32.2% and a maximum bending angle of 80 deg. [DOI: 10.1115/1.4050097]

Keywords: compliant mechanisms, mechanism design, parallel platforms, soft robots

1 Introduction

Inspired by nature, continuum robots, especially continuum manipulators, are developed to achieve animal-like compliant-to-object property. This property is thought critical for certain applications that require passive compliance, for instance, medical robots that need to interact with human tissues, manipulation robots that need to handle fragile objects, or exploration robots that need to go through unexpected narrow passages. Traditional solutions for this type of robot focus on using deformable materials (e.g., an elastic backbone) and/or deformable actuation (e.g., tendon or rod driven). Existing examples using this technology include the Elephant trunk [1], the Tentacle robot [2], and the DDU [3], etc. Another solution is to use a hyperredundant structure, which is not theoretically a continuum robot but can behave like one. The proposed design utilizes traditional serially connected rigid link structures and usually distributes/transmits the actuation on each joint. The typical representations for this category are snake-like robots [4–6] and multilink tail robots [7–9].

Limited by the mechanical structure and the actuation technology, the aforementioned solutions are usually not extensible (which are referred to as tail-like spatial bending mobility in this article). However, for certain applications where the manipulator base motion is constricted or disabled, an additional worm-like extensibility (self-extension mobility) can significantly augment its manipulability and dexterity.

Motivated by this observation, this article proposed a new mechanism that enables the continuum manipulator to bend and extend simultaneously. An extensible continuum manipulator (ECM)

based on this mechanism was designed and integrated. Both the mechanism and the manipulator are the first ones of their kind, which use motion propagation mechanisms to achieve extension mobility. An overview of the prototype is shown in Fig. 1. This new manipulator is envisioned to have potential applications in minimally invasive surgery, tentacle-like manipulations, as well as for search and rescue tasks (as a novel snake robot design).

The following sections are organized as follows. Section 2 reviews the existing technological background and the design motivations of this study. Section 3 describes the mechanical design of the robot system. Section 4 formulates the kinematics based on constant curvature bending assumption and conducts workspace analysis as well as motion nonuniformity evaluation accordingly. Section 5 presents the prototyping details and experimental results. Section 6 recaps the main points of this article and discusses the future work.
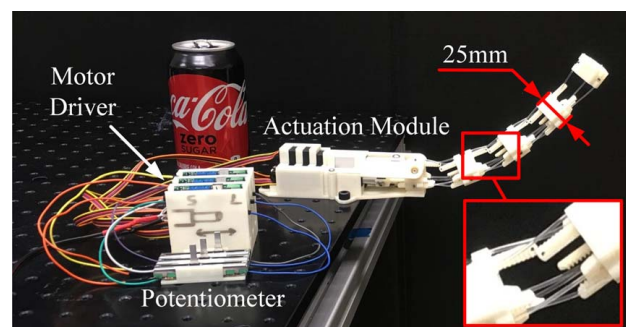
Fig. 1 Proof-of-concept prototype of the new extensible continuum manipulator

Journal of Mechanisms and Robotics   JUNE 2021, Vol. 13 / 031014-1

2 Background and Design Motivation

This section reviews the existing technologies for extensible continuum manipulator designs and presents the previously proposed rigid coupling hybrid mechanism (RCHM) concept, which is the foundation of the new mechanism presented in this paper.

2.1 Extensible Continuum Manipulator Review. To realize the extension mobility on traditional continuum robots, the easiest way might be converting the nonextensile backbone structure into an extensible one. The existing approaches that apply this idea include the NASA tendril type robots [10–13], which use extension and compression springs as the backbone, the tendon-driven continuum robot [14], which takes advantage of the magnetic repulsion force for backbone extension, the extensible continuum robot [15] using origami modules, and the concentric tube robot [16]. However, except for the concentric tube robot, the extension motion of these manipulators is usually passive or not actuated (similarly, actuated extension is referred to as active), especially when a tendon-driven system is used. This shortcoming causes the manipulator stiffness to decrease significantly as the manipulator extends. The stiffness of the concentric tube robot, although having active extension mobilities, is still uncontrollable due to the precurved tubes. Therefore, besides making the backbone extensible, a more straightforward way is to eliminate the backbone structure and use extensible actuators directly, such as a pneumatic actuator or an artificial muscle [17]. This approach avoids the passive extension disadvantages but introduces other shortcomings, such as the need for a heavy and unstable pneumatic actuators. More importantly, without the backbone, the manipulator becomes a tentacle, which has limited usages for carrying a load or applying force control.

Therefore, looking for a new continuum robot mechanism that has both a stronger backbone and an active extension, mobility becomes a promising direction for continuum robotics research. To achieve this goal, one existing solution is to use the RCHM concept, which was originally proposed to design spatial curvature bending mechanisms based on rigid links [18]. These types of mechanisms take advantage of the traditional hybrid mechanism structure [19], but use specific transmission mechanisms to couple adjacent subsegment mechanisms. Following this novel mechanism design idea, extension mobility for continuum manipulators could be added by designing special subsegment parallel mechanisms (PMs).

2.2 Rigid Coupling Hybrid Mechanism. As the theoretical foundation of the mechanism design in this article, it is worth to present the basic RCHM knowledge before going into the design details. As shown in Fig. 2, the core idea of this mechanism is to take advantage of the motion from the i-th link to drive the $(i+1)$-th link instead of transmitting motion directly from the base to each link. Such method of motion transmission is realized by "coupling" the $(i+1)$-th link with the i-th link using a rigid transmission mechanism (RTM). For the basic mobility of each subsegment, traditional PMs are used. Therefore, combining these two mechanism components, the new hybrid mechanism can amplify the subsegment mobility to the manipulator scale. Using the notations in Fig. 2, the overall motion sequence is described as follows. The actuators first drive the PM1 to achieve the desired subsegment motion. The RTM1 then duplicates the PM1 motion to drive PM2. After PM2 moves, RTM2 transmits the motion from PM2 to drive PM3 and so on. In practice, depending on the mobility requirement, existing parallel robot mechanisms could be directly used as the PM design, for instance, using the P̲S-P̲R mechanism for a 2DOF motion or using the 3P̲RS mechanism for a 3DOF motion. In the aforementioned and the following mechanism representations, "P" stands for prismatic joint, "R" stands for revolute joint, and "S" stands for spherical joint (which is also referred to as a ball joint). The underline beneath the letter indicates an actuated
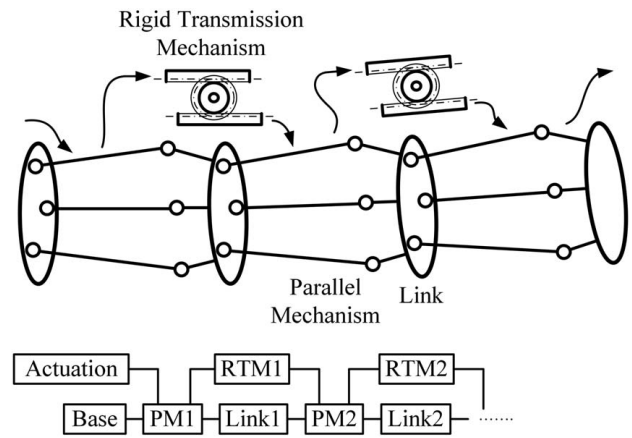

Fig. 2 The illustrative (top) and topological (bottom) diagrams of the rigid coupling hybrid mechanism concept

joint. In comparison with the vast PM design candidates, the RTM design has very limited options. The most frequently used RTMs are four-bar mechanism, rack and pinion set, slider mechanism for transmitting translational motion, and a universal shaft or a gear set for transmitting rotational motion.

The RCHM has two main advantages in comparison with the traditional cable-driven hyper-redundant designs: (1) the RCHM usually has good rigidity due to the parallel mechanism used for each subsegment, which is known to have higher stiffness, higher precision, and better load-bearing capability than its serial counterpart; (2) the usage of rigid link transmission in the RCHM avoids the commonly observed cable-driven issues, such as the unidirectional driving problem and the cable tension control problem. These two features, together, provide the RCHM with good rigidity and enable the mechanism to respond to high-frequency input, which is critical for applications that need high-speed or high dynamic motion. Second, since the RCHM has centralized actuation, the weight of the robot itself could be significantly reduced. As a result, the motion accuracy of the robot could be increased, and the controller could be simplified.

3 Mechanical Design

This section details the mechanical design of the new extensible manipulator. Since the RCHM design is based on rigid link transmission, to meet the mobility requirement, the PM is first synthesized using rigid links and then modified to use flexible links.

3.1 Parallel Mechanism Design Using Flexible Parallel Mechanism. The first step for the RCHM design is to select the appropriate PM to realize the subsegment motion, which is the 2R1 T (two radial rotations and one axial translation) motion in this case. There are many existing researches on the mechanism synthesis for this motion [20], among which the simplest might be the 3P̲SR mechanism [21]. However, to take advantage of the motion generated by this 3P̲SR mechanism and transmit motion to the next subsegment, another three chains are required. These three additional chains are placed close to the three original chains, respectively, so that each additional chain behaves simultaneously and similarly with its original chain counterpart. This way, the additional chains are able to "measure" the motion generated by the original chains. Therefore, these three additional chains are usually called "Measuring PM," while the original three chains are called "Driving PM" due to their different functionalities. It is important to note that due to the physical thickness of the links, the closeness of the additional chain with the original chain could never become zero, which leads to the fact that the "Measuring PM" could never exactly copy the motion of the "Driving PM."
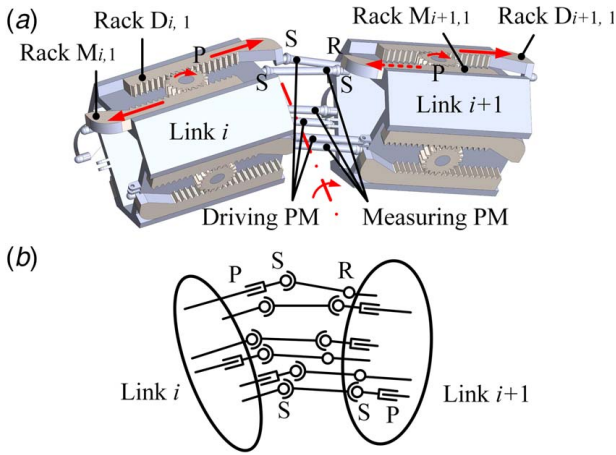
Fig. 3 (a) The original PM design using rigid links and rigid joint and (b) the corresponding kinematic diagram of the PM

Fig. 4 The modified PM design that uses flexible rods to replace the rigid links and rigid joints. A local section view of link i shows the internal rack and pinion transmission mechanism.

As a result, this fact brings in nonuniform twist motions (the non-uniformity could be very small if the two chains were designed to be close enough) among subsegments. More details about this will be discussed in Sec. 4.4.

Since the "Driving PM" is already fully constrained, the three additional chains cannot exert more constraints onto the system. Therefore, three spherical-spherical-prismatic (SSP) chains are selected to guarantee enough degrees-of-freedom for the "Measuring PM." Figure 3(a) shows one potential subsegment design based on this mechanism configuration, and Fig. 3(b) shows the corresponding kinematic diagram. The overall mobility can be verified by the Grübler–Kutzbach criterion (G-K criterion) [22] as follows:

$$
\begin{aligned}
M &= 6n - \sum_{i=1}^{j} (6 - f_i) \\
&= 6 \times 13 - 3 \times (5 + 3 + 5) - 3 \times (3 + 3 + 5) = 6
\end{aligned}
\quad (1)
$$

where n is the number of moving bodies, j is the number of joints, and f_i is the corresponding degree-of-freedom (DOF) of joint i. Although the calculation shows the mechanism having 6DOF, three of them are actually internal DOF (self-rotation with respect to the axis connecting the two ball joint centers) induced by the spherical-spherical (SS) chains, which do not affect the overall mobility. Therefore, the actual mobility of the 3PSR-3SSP mechanism is 3.

The PM together with the rack and pinion transmission forms the basic motion propagation mechanism. For instance, referring to Fig. 3(a), if an input motion (indicated by the solid arrow) is exerted on Rack $M_{i,1}$, Rack $D_{i,1}$ is pushed right through the gear. This motion causes the clockwise rotation of Link $i + 1$, which further induces the relative motion of $M_{i+1,1}$ (indicated by the dashed arrow). Because of the gear, this relative motion continues to be transmitted onto Rack $D_{i+1,1}$, which becomes the driving motion for the next subsegment.

Using rigid links and joints provides the advantages of being able to bear a larger load and having higher stiffness. The disadvantages include complicated mechanical structure that makes the manufacturing process more challenging in terms of manufacturing tolerance control problems (e.g., the backlash is rapidly amplified due to the motion propagation characteristics of this type of mechanism). Therefore, flexible parallel mechanisms [23,24] (FPMs) are proposed to replace the rigid link-based PM. The flexible structure facilitates the manufacturing process significantly and increases the accuracy by avoiding backlash (i.e., the deformation of the material itself does not induce backlash). Moreover, the flexible structure has the same compliant-to-obstacle benefit as traditional continuum robots.
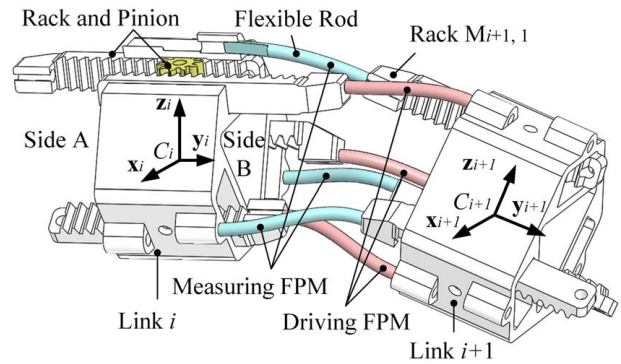
As shown in Fig. 4, the modified subsegment design uses flexible rods to replace the original rigid links and joints. Similarly, the six-chain FPM is subdivided into one "Driving FPM" and one "Measuring FPM." After changing to flexible rods, the mounting and connection among parts become easier too. For instance, the rods could be easily connected with the racks and the links using glue. The rack and pinion sets are also placed internally to achieve better assembly accuracy.

3.2 System Assembly. Figure 5 shows the overall design of the new ECM, where the ECM body is composed of four serially connected subsegments. Customized housing covers are designed to mount three linear actuators. The connection between the actuation module and the ECM body is achieved by a specifically designed first link and three special racks. To facilitate adding more subsegments to the ECM, the rest of the links and racks are designed to be identical. This modular design feature also allows extending the one segment design to multiple segments design, which could significantly increase the manipulator's workspace and enhance its dexterity.

It is worth to note that the size of the ECM body is mainly constrained by the gear teeth modulus. Using a smaller gear modulus allows designing smaller links without introducing significant twist effects (will be discussed in Sec. 4.4) and thus reduces the overall manipulator thickness. The current design uses the common 0.5 modulus gears, which limits the manipulator thickness to be 25 mm. In future designs, if smaller module gears (e.g., 0.2 modulus gears) are used, the manipulator thickness could be reduced to 15 mm, which would enable the ECM to be a good candidate for minimally invasive surgical applications.

4 Kinematic Analysis

For the preliminary kinematic analysis, certain assumptions could be made to simplify the computation. Due to the similar
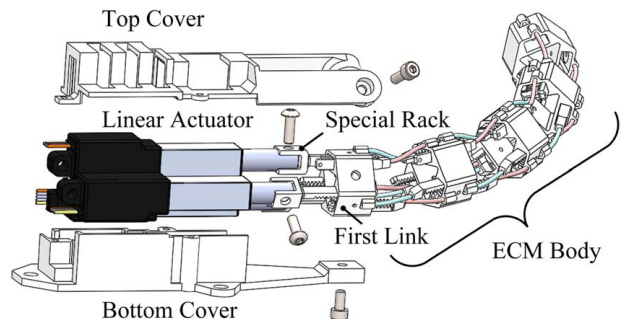
Fig. 5 Overall design of the new ECM
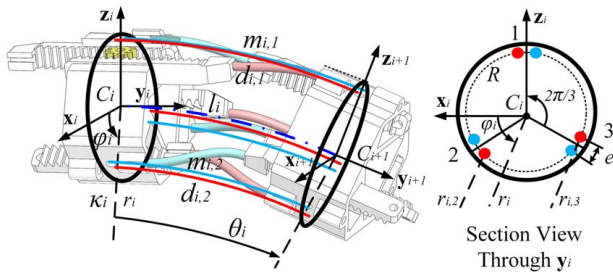
Fig. 6 Subsegment kinematic model based on the circular arc bending assumption

mobility as in the traditional extensible continuum manipulator, the circular arc bending assumption [25] is made here. That is, each subsegment is regarded as a constant curvature bending continuum robot section, and each rod together with its rack is regarded as the driving cable/rod for that continuum robot section. This way, each subsegment shape is fully defined by the three chains in the "Driving FPM," and the three chains in the "Measuring FPM" only measure the corresponding arc length and transmit it to the next subsegment.

4.1 Subsegment Kinematics. Figure 6 illustrates the subsegment kinematic model based on the circular arc bending assumption, where the driving arcs (in the section view, each of these arcs corresponds to the dot on the counterclockwise direction of each dot pair) are the abstraction of the driving chains with length $d_{i,j}$ and the measuring arcs (corresponding to the dots on the clockwise direction of the dot pairs in the section view) are the abstraction of the measuring chains with length $m_{i,j}$. $i \in \{1, 2, 3, 4\}$ represents the i-th link and $j \in \{1, 2, 3\}$ represents the jth chain in one subsegment. Body fixed frame $\sum C_i = (C_i, \mathbf{x}_i, \mathbf{y}_i, \mathbf{z}_i)$ is placed at the center of the i-th link. l_i, κ_i, r_i, and θ_i denote the arc length, curvature, radius, and central angle for the central bending arc (in dash-dot line), respectively. φ_i is the angle of the bending plane from $\mathbf{x}_i$ axis, and R is the distance of the driving/measuring arcs from the central arc. Based on mathematical definitions, the following relationships are self-satisfied:

$$l_i = \theta_i r_i \tag{2}$$

$$r_i = 1/\kappa_i \tag{3}$$

Therefore, with three arc lengths $d_{i,j}$, the bending shape is fully determined. The forward kinematics is obtained in the same way as in Ref. [25]:

$$l_i = \frac{d_{i,1} + d_{i,2} + d_{i,3}}{3} \tag{4}$$

$$\kappa_i = \frac{2\sqrt{d_{i,1}^2 + d_{i,2}^2 + d_{i,3}^2 - d_{i,1}d_{i,2} - d_{i,1}d_{i,3} - d_{i,2}d_{i,3}}}{R(d_{i,1} + d_{i,2} + d_{i,3})} \tag{5}$$

$$\varphi_i = -\text{atan2}\left(d_{i,3} + d_{i,2} - 2d_{i,1}, \sqrt{3}(d_{i,3} - d_{i,2})\right) + \frac{e}{2R} \tag{6}$$

where the second term in Eq. (6) is the angle shift due to the mounting point offset of the driving arc on the sectional view plane (the dots are not exactly located on the $\mathbf{z}_i$ axis).

Knowing the bending shape, the three measuring arc lengths could be obtained by inverse kinematics as follows:

$$m_{i,j} = l_i - l_i \kappa_i R \cos\left(\varphi_i + \frac{e}{2R} + \frac{7\pi}{6} - \frac{2\pi}{3}j\right) \tag{7}$$

For the $(i+1)$-th subsegment, the driving arc length should be replaced by the measuring arc length from the i-th subsegment. That is,

$$d_{i+1,j} = m_{i,j} \tag{8}$$

Note that the aforementioned and the following equations do not include the $\kappa_i = 0$ cases, which could be easily handled in actual programming by manually assigning values to all the variables.

4.2 Overall Kinematics. The overall kinematic model could be easily obtained as long as the subsegment wise kinematics is known. That is, with l_i, κ_i, and φ_i known, the vector from C_i to C_{i+1} is obtained as follows:

$$\mathbf{p}_{i,i+1} = r_i \sin\theta_i \mathbf{y}_i + (r_i - \cos\theta_i r_i)(\cos\varphi_i \mathbf{x}_i - \sin\varphi_i \mathbf{z}_i) \tag{9}$$

The rotation from $\sum C_i$ to $\sum C_{i+1}$ is formulated as follows:

$$^{i}\mathbf{R}_{i+1} = e^{\theta_i \hat{\xi}} \tag{10}$$

where $\boldsymbol{\xi} = -\sin\varphi_i \mathbf{x}_i - \cos\varphi_i \mathbf{z}_i$ is the rotation axis vector and the hat above $\boldsymbol{\xi}$ indicates the skew-symmetric expansion. Equation (10) could be easily evaluated by Rodrigues' formula [26] as follows:

$$^{i}\mathbf{R}_{i+1} = \mathbf{I} + \sin\theta_i \hat{\xi} + \hat{\xi}^2(1 - \cos\theta_i) \tag{11}$$

With local displacement $\mathbf{p}_{i,i+1}$ and $^{i}\mathbf{R}_{i+1}$ known, the global displacement of $\sum C_i$ can be obtained recursively

$$\mathbf{p}_i = \mathbf{p}_{i-1} + \mathbf{p}_{i-1,i} \tag{12}$$

$$\mathbf{R}_i = ^{i-1}\mathbf{R}_i \mathbf{R}_{i-1} \tag{13}$$

with the initial displacement of $\mathbf{p}_1 = 0$ and $\mathbf{R}_1 = \mathbf{I}$.

4.3 Workspace Analysis. The workspace of the new ECM is defined by all the points that the manipulator tip can reach in 3D space. Based on the prototype measurements ($R = 25$ mm, d is from 42 mm to 62 mm, and $e = 2.3$ mm) and aforementioned kinematic analysis, the workspace is generated and presented in Fig. 7. As shown in this figure, the ECM workspace is a volume with three ridges appearing on both the concave and the convex surfaces. These ridges correspond to the cases that one or two actuators are in their extreme positions. As a contrast, the nonextensible counterpart (2DOF manipulator) of the ECM can only generate a surface for the workspace. More details of this case could be found in Ref. [18].

The workspace shows that the fully shortened manipulator has a length of 176 mm, and the fully extended case has a length of 256 mm. The maximal extension ratio (for what percentage the ECM can extend the most) is $(256 - 176)/176 = 45.45\%$. Note that since the workspace is generated purely based on the simplified kinematic model, the workspace analysis accounting for static metrics (e.g., pose accuracy, load capacity) is not applicable here.
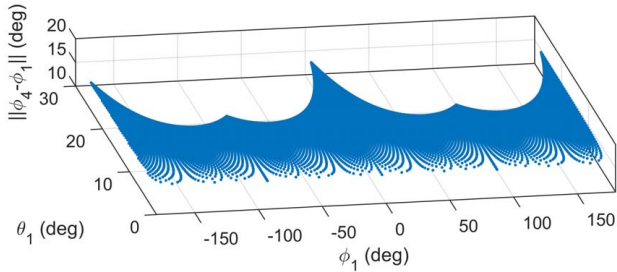
4.4 Motion Nonuniformity Evaluation. As discussed in Sec. 3.1, due to the rod mounting angle shift $e/R \neq 0$, the "Measuring PM" cannot exactly copy the "Driving PM" motion. This fact leads to a twist motion along the manipulator axial direction, which breaks the desired uniform motion for each subsegment. To evaluate the nonuniformity induced by this phenomenon, different angle shift e/R values are tested and the corresponding manipulator configurations with the same inputs ($d_{1,1} = 42$ mm, $d_{1,2} = 52$ mm, and $d_{1,3} = 52$ mm) are plotted in Fig. 8, in which five
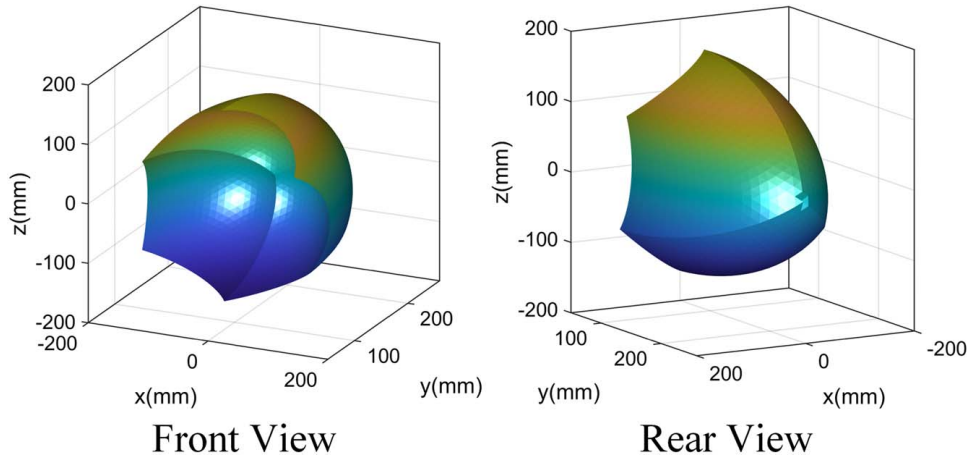
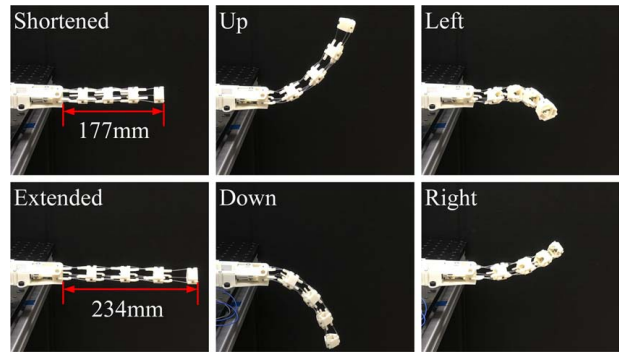**Fig. 7 Workspace of the new ECM. The interpolated colors and light effects are used for better visualization.**
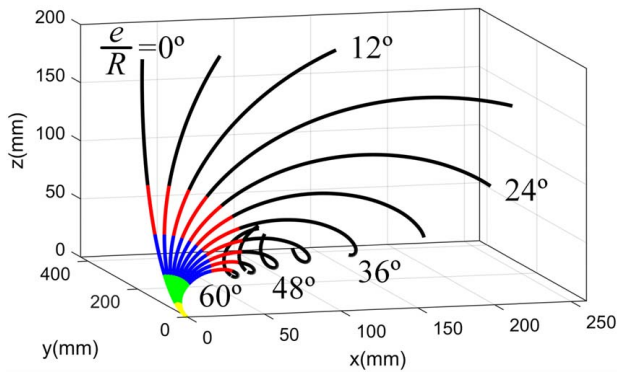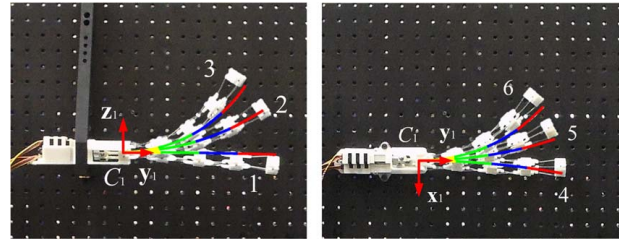

Fig. 8 Twist effect for different e/R values

Fig. 9 Distribution of nonuniformity for different ECM configurations

Fig. 10 The new ECM mobility demonstration

Fig. 11 Comparison of the actual manipulator shapes with the estimated shapes (smooth arcs) based on the kinematic model

additional subsegments (in black) are added to make the twist motion more visible. The other colors indicate the four subsegments in the actual design.

As shown in Fig. 8, the twist effect becomes quite significant as e/R is beyond 10 deg and more subsegments worsen the situation significantly. Therefore, for practical design purposes, reducing e to a value as small as possible and choosing fewer subsegments help reduce the undesired twist motion. For the existing design with a minimized e value (2.3 mm), the twist effect is also evaluated for different manipulator configurations. The nonuniformity is defined by the difference between the last subsegment bending plane angle φ_4 and the first subsegment bending plane angle φ_1. The numerical calculation was conducted and plotted in Fig. 9, which surprisingly shows that the nonuniformity (the value in the

figure is 15.81 deg) is not affected by the manipulator configuration.

This can be verified analytically by substituting Eq. (8) into Eq. (6), which yields

$$-\tan\left(\varphi_{i+1} - \frac{e}{2R}\right) = \frac{m_{i,3} + m_{i,2} - 2m_{i,1}}{\sqrt{3}(m_{i,3} - m_{i,2})} \tag{14}$$

Substituting Eq. (7) into Eq. (14) and evaluating, Eq. (14) is simplified to

$$\varphi_{i+1} - \varphi_i = \frac{e}{R} \tag{15}$$

which means that the twist effect only depends on the rod mounting angle shift e/R and the subsegment number.

Table 1 Experimental data

Shape	Driving arc length $(d_{1,1}, d_{1,2}, d_{1,3})$ (mm)	Measured C_5 position (mm)	Computed C_5 position (mm)	Error norm (mm)
1	(57.3, 56.9, 57.2)	$(0, 229, -20)^T$	$(2.7, 228.6, -3.4)^T$	16.6
2	(51.7, 56.9, 57.2)	$(0, 220, 67)^T$	$(10.8, 209.1, 60.8)^T$	12.5
3	(47.8, 56.9, 57.2)	$(0, 178, 118)^T$	$(15.4, 182.8, 96.7)^T$	21.8
4	(54.8, 54.0, 55.9)	$(10, 220, 0)^T$	$(19.3, 218.5, -0.8)^T$	9.4
5	(52.9, 54.1, 50.8)	$(-53, 202, 0)^T$	$(-32.5, 207, -1.6)^T$	21.1
6	(53.8, 56.8, 48.1)	$(-102, 178, 0)^T$	$(-81.1, 189.2, -3.8)^T$	23.7

5 Prototyping and Experiments

To verify the proposed mobility of the new mechanism, a proof-of-concept prototype was built using acrylonitrile butadiene styrene-based 3D printing. Three Actuonix linear actuators (L12-30-210-6-P) with corresponding controller boards were used to drive the manipulator. For the rack and pinion transmission, off-the-shelf 0.5 modulus nylon gears were utilized, and customized racks were 3D printed. The flexible rods were made from Trik Fish lines with 1.35 mm diameter.

As shown in Fig. 10, the prototype exhibits the proposed 2R1 T mobility, for which the most shortened length is measured as 177 mm and the most extended length as 234 mm. The extension ratio is computed to be 32.2%, which is smaller than the ratio predicted by the workspace analysis. This is partially due to the smaller range applied on the linear actuator to avoid potential damage to the prototype. The maximal bending angle was measured to be around 80 deg. The prototype was also tested for its load capacity using a scale with 1 g precision. For the fully shortened configuration, the manipulator tip can generate a radial force of up to 59 g (around 0.58N) and an axial force of up to 671 g (around 6.6N) before significant buckling failure occurs.

To further evaluate the accuracy of the kinematic model, two sets of experiments were conducted. The first set measured three arbitrary shapes of the ECM on the $y_1 C_1 z_1$ plane using one stationary camera (Samsung HMX-F90 with 1696×954 pixels). The camera was placed 1.5 m away from a vertical pegboard (25 mm hole pattern), on which the manipulator base was fixed. The camera pose was adjusted carefully, so that the camera frame is parallel to the pegboard plane. The second set measured another three static shapes on the $x_1 C_1 y_1$ plane using the same camera setup. Due to the relatively large distance between the camera and the measuring plane, the distortion effect of the camera was neglected. Therefore, the world coordinates of the manipulator points could be measured by manually finding out the pixel coordinates on the image [27]. After calibrating with a checkerboard, this method could reach an accuracy of ± 3 pixels, which corresponds to ± 2 mm in the world coordinates on the measuring plane. Figure 11 shows the measurement results, where the three shapes of each experiment set were combined in one image. The estimated shapes based on the kinematic model are also plotted in the same figure. Note that the superimposition of images from the experiments and the images from the theoretical computations are rough and only meant to provide intuitive impressions on how large the error is. For accurate image composition, a rigorous process of mapping the theoretical data in the world coordinate into the pixel coordinates in the camera frame would be needed. The detailed measurement results are reported in Table 1, where the driving arc lengths are measured indirectly by recording the corresponding rack positions using a caliper. Since the single camera-based measurement cannot provide depth information, the unmeasurable components in the second column are set to zero and other components are rounded to the nearest integer. The error norm was also computed only for the measurable components. Based on the experimental data, the current kinematic model shows good accuracy in estimating the relative positions of the manipulator (bending shapes) but requires improvements in the absolute position estimation. The mismatch between the theoretical predictions and the experimental results is partly due to the fact that the flexible rods bend in a more complicated way when the manipulator approaches its extreme poses. This complicated bending behavior violates the circular arc assumption and thus causes the error. Another important reason contributing to the mismatch is the large friction that exists in the prototype (due to the usage of plastic gears and the lack of bearings). The friction forces the rods to bend more than the ideal case. Therefore, as more efforts will be directed to improve the prototype in the future, the friction could be reduced, and the kinematic model would be expected to have better prediction results.

Although the prototype demonstrates consistent bending shapes in general, the first subsegment was observed to have larger bending angles than the rest. The reason was partly due to the non-uniform motion effect that was discussed in Sec. 4.4. But more importantly, the nonuniformity for the first subsegment comes from its large driving force. As shown earlier, the new manipulator mechanism utilizes motion propagation as a way to transmit motion from the base to the tip link. Based on conservation of energy, this method will accumulate and amplify the driving force from each subsegment onto the first subsegment, which makes its flexible rods to deform more than those of the rest. If this force becomes too large, the flexible rods may not be able to stably transmit the axial force and may result in a sudden loss of stability, also known as the buckling phenomenon. Therefore, to analyze these behaviors and to better estimate the manipulator shape, a more accurate statics-based kinematic model (such as the modeling method used in Ref. [24]) is required for future work.

6 Conclusion and Future Work

By leveraging the rigid coupling hybrid mechanism concept and the flexible parallel mechanisms, a new 3DOF extensible continuum manipulator with spatial bending (2R) and one axial extension (1 T) mobility was proposed. The core idea lies in using the motion of the i-th link to drive the $(i+1)$-th link, so that the local motion can be copied and propagated from the base link to the tip link. To achieve this design goal, flexible parallel mechanisms were used to realize the basic 2R1 T subsegment motion, and rack and pinion sets were used to couple the adjacent subsegments. This way, the 2R1 T motion is copied by each subsegment and the entire manipulator achieves spatial bending and one extension mobility. To calculate the configuration of this new mechanism, a simplified kinematic model was formulated. The workspace analysis based on the kinematic model showed that the new manipulator is able to generate a volumetric workspace in comparison to the superficial workspace that its nonextensible counterparts generate. A small-scale proof-of-concept prototype was manufactured to validate the proposed mobility. Preliminary tests showed that the current design is able to extend 32% of its original length and bend over 80 deg. The manipulator can also generate a radial force of up to 0.58N and an axial force of up to 6.6N at its tip. Additional experiments on position accuracy showed that the simplified kinematic model can correctly predict the bending shape of the

manipulator but has a noticeable error on the absolute position estimation.

For future work, since the neglection of the static effects caused error in the kinematic analysis, one important focus is to develop a more accurate kinematic model based on the Coserrat rod theory, which will take into account the gravity, friction, and external loads. Moreover, improving the mechanical design to reduce the prototype friction (e.g., using metal gears and racks with smaller modulus) will also be an important part of the future work. Considering the potential applications of the new manipulator on medical robotics, the team will also work on the miniaturization of the mechanical design.

Funding Data

Conflict of Interest

There are no conflicts of interest.

Data Availability Statement

The datasets generated and supporting the findings of this article are obtainable from the corresponding author upon reasonable request. The authors attest that all data for this study are included in the paper.

References

[1] Hannan, M. W., and Walker, I. D., 2003, "Kinematics and the Implementation of an Elephant's Trunk Manipulator and Other Continuum Style Robots," J. Rob. Systems, 20(2), pp. 45–63.
[2] Li, C., and Rahn, C. D., 2002, "Design of Continuous Backbone, Cable-Driven Robots," ASME J. Mech. Des., 124(2), pp. 265–271.
[3] Simaan, N., Taylor, R., and Flint, P., 2004, "A Dexterous System for Laryngeal Surgery," IEEE International Conference on Robotics and Automation, New Orleans, LA, Apr. 26–May 1, pp. 351–357.
[4] Chirikjian, G. S., and Burdick, J. W., 1995, "Kinematically Optimal Hyper-Redundant Manipulator Configurations," IEEE Trans. Rob. Autom., 11(6), pp. 794–806.
[5] Wright, C., Johnson, A., Peck, A., McCord, Z., Naaktgeboren, A., Gianfortoni, P., Gonzalez-Rivero, M., Hatton, R., and Choset, H., 2007, "Design of a Modular Snake Robot," IEEE/RSJ International Conference on Intelligent Robots and Systems, San Diego, CA, Oct. 29–Nov. 2, pp. 2609–2614.
[6] Racioppo, P., and Ben-Tzvi, P., 2019, "Design and Control of a Cable-Driven Articulated Modular Snake Robot," IEEE/ASME Trans. Mech., 24(3), pp. 893–901.
[7] Liu, Y., Wang, J., and Ben-Tzvi, P., 2019, "A Cable Length Invariant Robotic Tail Using a Circular Shape Universal Joint Mechanism," ASME J. Mech. Rob., 11(5), p. 051005.
[8] Rone, W. S., Saab, W., and Ben-Tzvi, P., 2018, "Design, Modeling, and Integration of a Flexible Universal Spatial Robotic Tail," ASME J. Mech. Rob., 10(4), p. 041001.
[9] Saab, W., Rone, W. S., Kumar, A., and Ben-Tzvi, P., 2019, "Design and Integration of a Novel Spatial Articulated Robotic Tail," IEEE/ASME Trans. Mech., 24(2), pp. 434–446.
[10] Mehling, J. S., Diftler, M. A., Chu, M., and Valvo, M., 2006, "A Minimally Invasive Tendril Robot for In-Space Inspection," 1st IEEE/RAS-EMBS International Conference on Biomedical Robotics and Biomechatronics, Pisa, Italy, Feb. 20–22, pp. 690–695.
[11] Yang, J., Jason, P., and Abdel-Malek, K., 2006, "A Hyper-Redundant Continuous Robot," IEEE International Conference on Robotics and Automation, Orlando, FL, May 15–19, pp. 1854–1859.
[12] Velasquez, C. A., King, H. H., Hannaford, B., and Yoon, W. J., 2012, "Development of a Flexible Imaging Probe Integrated to a Surgical Telerobot System: Preliminary Remote Control Test and Probe Design," 4th IEEE RAS & EMBS International Conference on Biomedical Robotics and Biomechatronics, Rome, Italy, June 24–27, pp. 894–898.
[13] Frazelle, C. G., Kapadia, A. D., and Walker, I. D., 2020, "A Haptic Continuum Interface for the Teleoperation of Extensible Continuum Manipulators," IEEE Rob. Automation Lett., 5(2), pp. 1875–1882.
[14] Nguyen, T. D., and Burgner-Kahrs, J., 2015, "A Tendon-Driven Continuum Robot With Extensible Sections," IEEE/RSJ International Conference on Intelligent Robots and Systems, Hamburg, Germany, Sept. 28–Oct. 2, pp. 2130–2135.
[15] Zhang, K., Qiu, C., and Dai, J. S., 2016, "An Extensible Continuum Robot With Integrated Origami Parallel Modules," ASME J. Mech. Rob., 8(3), p. 031010.
[16] Webster, R. J., III, Romano, J. M., and Cowan, N. J., 2008, "Mechanics of Precurved-Tube Continuum Robots," IEEE Trans. Rob., 25(1), pp. 67–78.
[17] Jones, B. A., and Walker, I. D., 2006, "Kinematics for Multisection Continuum Robots," IEEE Trans. Rob., 22(1), pp. 43–55.
[18] Liu, Y., and Ben-Tzvi, P., 2020, "Design, Analysis, and Integration of a New Two-Degree-of-Freedom Articulated Multi-Link Robotic Tail Mechanism," ASME J. Mech. Rob., 12(2), p. 021101.
[19] Tanev, T. K., 2000, "Kinematics of a Hybrid (Parallel-Serial) Robot Manipulator," Mech. Mach. Theory, 35(9), pp. 1183–1196.
[20] Fan, C., Liu, H., and Zhang, Y., 2013, "Type Synthesis of 2T2R, 1T2R and 2R Parallel Mechanisms," Mech. Mach. Theory, 61, pp. 184–190.
[21] Li, Q., and Hervé, J. M., 2010, "1T2R Parallel Mechanisms Without Parasitic Motion," IEEE Trans. Rob., 26(3), pp. 401–410.
[22] Gogu, G., 2005, "Mobility of Mechanisms: a Critical Review," Mech. Mach. Theory, 40(9), pp. 1068–1097.
[23] Wang, X., and Mills, J. K., 2006, "Dynamic Modeling of a Flexible-Link Planar Parallel Platform Using a Substructuring Approach," Mech. Mach. Theory, 41(6), pp. 671–687.
[24] Black, C. B., Till, J., and Rucker, D. C., 2017, "Parallel Continuum Robots: Modeling, Analysis, and Actuation-Based Force Sensing," IEEE Trans. Rob., 34(1), pp. 29–47.
[25] Webster, R. J., III, and Jones, B. A., 2010, "Design and Kinematic Modeling of Constant Curvature Continuum Robots: A Review," Int. J. Rob. Res., 29(13), pp. 1661–1683.
[26] Kurdila, A. J., and Ben-Tzvi, P., 2019, Dynamics and Control of Robotic Systems, John Wiley & Sons, Hoboken, NJ.
[27] Godage, I. S., Medrano-Cerda, G. A., Branson, D. T., Guglielmino, E., and Caldwell, D. G., 2016, "Dynamics for Variable Length Multisection Continuum Arms," Int. J. Rob. Res., 35(6), pp. 695–722.